

Food & Function

Accepted Manuscript

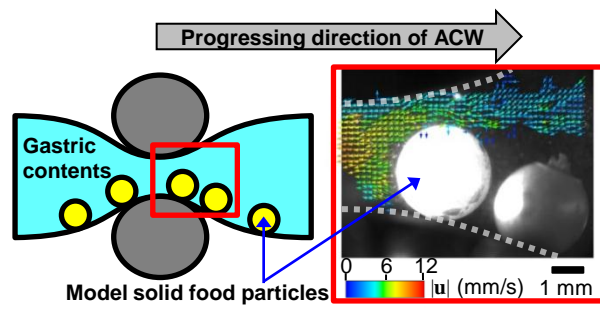


This is an *Accepted Manuscript*, which has been through the Royal Society of Chemistry peer review process and has been accepted for publication.

Accepted Manuscripts are published online shortly after acceptance, before technical editing, formatting and proof reading. Using this free service, authors can make their results available to the community, in citable form, before we publish the edited article. We will replace this *Accepted Manuscript* with the edited and formatted *Advance Article* as soon as it is available.

You can find more information about *Accepted Manuscripts* in the [Information for Authors](#).

Please note that technical editing may introduce minor changes to the text and/or graphics, which may alter content. The journal's standard [Terms & Conditions](#) and the [Ethical guidelines](#) still apply. In no event shall the Royal Society of Chemistry be held responsible for any errors or omissions in this *Accepted Manuscript* or any consequences arising from the use of any information it contains.



Graphical abstract

1 **PIV and CFD studies on analyzing intragastric flow phenomena induced by**
2 **peristalsis using a human gastric flow simulator**

3

4 Hiroyuki Koza^{1,2}, Isao Kobayashi^{1,*}, Marcos A. Neves^{1,2}, Mitsutoshi Nakajima^{1,2}, Kunihiko
5 Uemura¹, Seigo Sato², and Sosaku Ichikawa^{2,*}

6

7 ¹ *Food Engineering Division, National Food Research Institute, NARO, 2-1-12 Kannondai,*
8 *Tsukuba, Ibaraki 305-8642, Japan*

9 ² *Graduate School of Life and Environmental Sciences, University of Tsukuba, 1-1-1*
10 *Tennoudai, Tsukuba, Ibaraki 305-8572, Japan*

11

12 * Corresponding authors Tel: +81-29-838-8025; Fax: +81-29-838-8122; E-mail:
13 isaok@affrc.go.jp (I. Kobayashi), Tel: +81-29-853-4627; Fax: +81-29-853-4605; E-mail:
14 ichikawa.sosaku.fn@u.tsukuba.ac.jp (S. Ichikawa)

15

1 Abstract

2 This study quantitatively analyzed the flow phenomena in model gastric contents
3 induced by peristalsis using a human gastric flow simulator (GFS). Major functions of the
4 GFS include gastric peristalsis simulation by controlled deformation of rubber walls, and
5 direct observation of inner flow through parallel transparent windows. For liquid gastric
6 contents (water and starch syrup solutions), retroulsive flow against the direction of
7 peristalsis was observed using both particle image velocimetry (PIV) and computational fluid
8 dynamics (CFD). The maximum flow velocity was obtained in the region occluded by
9 peristalsis. The maximum value was 9 mm/s when the standard value of peristalsis speed in
10 healthy adults ($U_{ACW} = 2.5$ mm/s) was applied. The intragastric flow-field was laminar with
11 maximum Reynolds Number ($Re = 125$). The viscosity of liquid gastric contents hardly
12 affected the maximum flow velocity in the applied range of this study (1 to 100 mPa s). These
13 PIV results agreed well with the CFD results. The maximum shear rate in the liquid gastric
14 contents was below 20 s^{-1} at $U_{ACW} = 2.5$ mm/s. We also measured the flow-field in solid-liquid
15 gastric contents containing model solid food particles (plastic beads). The direction of
16 velocity vectors was influenced by presence of the model solid food particles surface. The
17 maximum flow velocity near the model solid food particles ranged from 8 to 10 mm/s at U_{ACW}
18 $= 2.5$ mm/s. The maximum shear rate around the model solid food particles was low, with a
19 value of up to 20 s^{-1} .

20

21 **Keywords:** Gastric peristalsis, Flow-field, Shear force, Multi-phase, PIV, CFD

1. Introduction

Ingested foods undergo physical, chemical, and biological digestive processes in the mouth, stomach, and small and large intestines. Investigating food disintegration and absorption in human digestive organs can provide insight into food digestion phenomena, which may lead to better control of food digestibility. The functions of the stomach, the major digestion organ, include physical digestion by gastric peristalsis, as well as chemical digestion by gastric juice. The physical digestive process involves grinding food into small particles, mixing gastric contents consisting of food and gastric juice, and emptying chyme into the duodenum. The intragastric hydrodynamic phenomena caused by peristalsis are assumed to promote enzymatic hydrolysis and shearing of foods.¹ Such basic hydrodynamic knowledge is essential for understanding food digestion phenomena.

Antral contraction waves (ACWs), which induce intragastric flow phenomena, are generated on the gastric wall and progress toward the pylorus, which is at the end of the stomach. The generation and motion of ACWs have been clinically observed mainly using magnetic resonance imaging (MRI).² Previous studies have indicated that fluid motions in the stomach promote emulsification of oil components, as well as drug release from matrix tablets.^{3,4} Also, *in vivo* MRI study demonstrates that gastroparesis patients exhibit unusual peristaltic motion, decreasing U_{ACW} , or different degrees of ACW contractions.² However, the quantitative data on intragastric flow is not yet fully understood, because flow velocity or shear stress values cannot be measured.

Gastric digestion has also been studied using *in vitro* methods.^{5,6} Conventional *in vitro* gastrointestinal (GI) models utilize mixing gastric contents inside small vessels using a shaking or stirring device, focusing on the chemical environment in the actual stomach.⁶⁻⁸ Two automated complex *in vitro* GI devices have been developed in the last two decades: the TNO gastrointestinal Model (TIM) and the Dynamic Gastric Model (DGM).^{9,10} These

1 devices can control the secretion of GI fluids, pH, temperature, and emptying, which is useful
2 for dynamically simulating the chemical digestive processes in the GI tract. Gastric contents
3 are mixed by water pressure (TIM) or water pressure and piston/barrel (DGM).¹¹ The Human
4 Gastric Simulator (HGS) developed by Kong & Singh can generate a progressing wave that
5 simulates ACW on a gastric wall made of opaque latex and a roller rotation system.¹²
6 However, the inner flow-field occurring during digestion experiments can depend on the type
7 of the GI devices used. For instance, conventional GI digestion methods cannot simulate the
8 flow-field induced by wall contraction (e.g., peristalsis). Also, all *in vitro* models were
9 designed for digestion experiments using real foods and drugs, not for flow-field
10 visualization.

11 Hydrodynamic phenomena induced by human peristalsis have been studied using mainly
12 *in silico* approaches involving the lattice Boltzmann and computational fluid dynamics (CFD)
13 methods.¹³⁻¹⁶ Pal *et al.* prepared a two-dimensional domain of the whole human stomach, and
14 calculated the intragastric flow of the single liquid phase.¹³ Their results suggest that there
15 were two characteristic intragastric flows: repulsive jet flow through ACWs and circulatory
16 flow behind ACWs. We previously analyzed the effects of fluid viscosity and enzyme mass
17 transfer in the intragastric flow-field.¹⁵ There is a great difference (10 times) in both
18 maximum intragastric flow velocity and average vorticity values reported in previous
19 publications when using the same viscosity of gastric contents.^{13,14} Also, calculating
20 multi-phase gastric contents containing solid particles is difficult because of the high
21 computational load and numerical instability due to the complex flow system. Though Ferrua
22 & Singh experimentally visualized intragastric flow, the effects of ACW parameters (U_{ACW} ,
23 shape, and frequency) on intragastric flow are still unclear.¹⁴ Also, the range of fluid viscosity
24 in their study was not great enough (1 to 18 mPa s), since the viscosity of actual gastric
25 contents may be higher than 100 mPa s.¹⁷ The flow-field in liquid-solid gastric contents is

1 difficult to measure in this system, as the gastric wall is placed vertical to bottom plane.
2 Therefore, it is necessary to perform more systematic analysis of the intragastric flow
3 phenomena, including both liquid and liquid-solid systems, using experimental and
4 computational approaches.

5 This study seeks to investigate the intragastric flow phenomena induced by human gastric
6 peristalsis using both *in vitro* and *in silico* analyses. To experimentally observe intragastric
7 flow, we developed an *in vitro* device, the simplified gastric flow simulator (GFS). This GFS,
8 which mimics the antrum, consists of parallel transparent walls on one plane and rubber
9 sidewalls on another plane for inducing ACWs. We experimentally investigated the flow-field
10 of liquid and liquid-solid gastric contents using particle image velocimetry (PIV) at different
11 ACW speeds (U_{ACW}). The effect of fluid viscosity on the flow-field was investigated using
12 starch syrup at various concentrations. The shear rate induced by peristalsis in the gastric
13 contents was estimated based on the flow-field obtained from PIV measurement. We also
14 conducted CFD calculation applying the same flow conditions as those used for PIV
15 measurement and compared the results.

16

17 **2. Materials and methods**

18 *2.1. Materials and fluid properties*

19 Starch syrup (B-75) was purchased from Kato Kagaku Co., Ltd. (Mihama, Japan). Starch
20 syrup dissolved in Milli-Q water, which is Newtonian fluid¹⁸, was used as model liquid
21 gastric contents: Milli-Q water (pH 5.8), Starch syrup (36% (v/v)) (pH3.6), Starch syrup (56%
22 (v/v)) (pH3.3). The physical properties of each model liquid gastric contents are listed in
23 Table 1. Density was measured using a density meter (DA-130 N, KEN Kyoto Electronics
24 Manufacturing Co., Ltd., Kyoto, Japan), and viscosity was measured using a Vibroviscometer
25 (SV-10, A&D Co., Ltd., Tokyo, Japan). Plastic beads made of urea formaldehyde resin were

1 purchased at a local market, to be used as model solid food particles. Considering the normal
2 size of food particles inside the stomach, 3 mm spherical plastic beads were selected.¹⁹ The
3 concentration of plastic beads used was less than 25% (v/v). The composition of liquid and
4 liquid-solid gastric contents is presented in Table 1.

5 Nylon particles with a diameter of 30 μm and a density of 1030 kg/m^3 were used as
6 tracer particles. It is important to determine whether the tracer particles follow the flow-field
7 generated by ACW in GFS. The Stokes number S (-), defined as the ratio of response time of
8 tracer particles and characteristic time of the applied flow, was estimated using Eq. 1:

$$S = \frac{\rho_p d^2 U}{18 \mu L} \quad (1)$$

9
10 , where ρ_p is density (kg/m^3) and d is diameter of tracer particles (m), U is the characteristic
11 flow velocity (m/s), μ is the fluid viscosity (Pa s), and L is the characteristic length (m).²⁰ U
12 was set to 10 mm/s, which is the maximum flow velocity in the gastric flow reported in our
13 previous study.¹⁵ μ was set to 0.91 mPa s as the minimum viscosity of liquid gastric contents
14 applied in this study. The characteristic length (30 mm) was based on the diameter of a
15 previous 2-D stomach model.¹⁵ The estimated maximum S was on the order of 10^{-5} , indicating
16 that the tracer particles applied in this study follow the fluid motion reasonably well.

17

18 2.2. PIV measurement

19 2.2.1. Gastric flow simulator

20 Figure 1a presents a three-dimensional drawing of the GFS developed for this study. The
21 deformable rubber walls on the top and bottom of the GFS simulate gastric walls. Other walls
22 made of transparent material (poly methyl metacrylate (PMMA)) were designed for easily
23 observing the motion of gastric contents. Peristaltic motion simulating ACW was generated
24 by pushing plastic rollers (30-mm diameter x 20-mm width) on the rubber walls and then

1 moving them towards the outlet that simulates the pylorus, represented by the 30-mm x
2 15-mm section on the right-hand side of Fig. 1a. The minimum clearance of the region
3 occluded by the deformed rubber walls was set to 3.0 mm. The U_{ACW} can be controlled by the
4 rotation of the motor connected to two rollers. The outlet of the GFS was closed during the
5 experiments. The inlet hole of the GFS (see Fig. 1a) was connected to a plastic tube open to
6 the air. A portion of the gastric contents in the GFS can move smoothly in the tube when an
7 ACW is generated on the rubber walls. Prior to each measurement, the GFS was filled with
8 model liquid contents (Fig. 1c, left) or model liquid-solid contents (Fig. 1c, right). The
9 volume ratio of model solid food particles for model liquid-solid gastric contents was varied
10 from 5% to 25%. During the experiments, ACWs moved toward the outlet at the U_{ACW} of
11 1.25, 2.5, or 5.0 mm/s. The standard U_{ACW} value for human ACW was reported to be 2.5
12 mm/s.¹³

13

14 2.2.2. Visualization system

15 The visualization system used in this study is illustrated in Fig. 1b. Tracer particles
16 (nylon particles) were seeded into the liquid phase at a concentration of 0.009wt% for Milli-Q
17 water or 0.03wt% for starch syrups. Light was irradiated from a PMMA window close to the
18 GFS inlet. A white light was used to illuminate the tracer particles for single-phase flow
19 analysis. A diode-pumped solid-state (DPSS) laser with a wavelength of 532 nm (M Square
20 Co., Ltd., Fukuoka, Japan) was used to illuminate tracer particles and model solid food
21 particles in two-phase flow analysis. This laser source can irradiate a light sheet with a depth
22 of 1.0 mm, allowing detailed analysis of the flow-field around model solid food particles. The
23 side-way scattered light of tracer particles illuminated by white light or green laser were
24 visualized using a high-speed video camera (FASTCAM SA 1.1, Photron Co., Ltd., Tokyo,
25 Japan) with a maximum frame rate of 250 fps, and their images were recorded in a computer.

1 The video camera was focused on the search plane indicated by the dotted line in Fig. 1b, and
 2 tracer particles that were out of focus were removed by image processing to obtain
 3 two-dimensional images of tracer particles on the search plane.

4

5 2.2.3. Data analysis

6 PIV image processing was performed using a direct cross-correlation algorithm. The
 7 recorded images containing tracer particles had a resolution of 1010 x 506 pixels for
 8 single-phase flow analysis or 986 x 746 pixels for two-phase flow analysis. The size of the
 9 interrogation area (IA) was set to 24 x 24 pixels with an overlap sampling rate of 50% for
 10 flow measurement in the liquid contents system (single-phase). The IA size was set to 40 x 40
 11 pixels for flow measurement in the liquid-solid contents system (two-phase), since the set
 12 magnification of the video camera in this case exceeded that for the single-phase flow. The
 13 number of tracer particles in each IA ranged from 2 to 5. The size of the search region was set
 14 to ± 13 pixels for all PIV measurements. The flow velocity vectors obtained by direct
 15 cross-correlation were post-processed using a local median filter to detect spurious vectors.²¹

16 The absolute value of the shear rate ($|\dot{\gamma}|$) induced by peristalsis was estimated using Eq. 2:

$$17 \quad |\dot{\gamma}| = \left| \frac{\partial u}{\partial y} + \frac{\partial v}{\partial x} \right| \quad (2)$$

18 , where u and v are x and y components of the flow velocity vector. The shear rate
 19 distribution was estimated based on the gradient of the flow velocity vectors. The
 20 second-order central difference based on the eight neighboring vectors of the local point was
 21 applied to estimate differential values in Eq. 2. Finally, the hydrodynamic shear stress (σ) was
 22 estimated by following Eq. 3:

$$23 \quad \sigma = \mu |\dot{\gamma}| \quad (3)$$

24 , where μ is the fluid viscosity.

1

2 *2.2 . CFD Simulations*

3 In this study, a numerical approach, Computational Fluid Dynamics (CFD), was also
 4 conducted to validate the results of flow-field obtained in PIV measurement. A CFD software
 5 package (CFD-ACE+ version 2008, ESI Group, Paris, France) was used for calculating the
 6 single-phase flow in the GFS. Details of the simulation method are described in our previous
 7 publication.¹⁵ The flow-field was calculated based on a finite volume method that solves the
 8 Navier-Stokes equation for incompressible fluids (Eq. 4) and the continuity equation (Eq. 5):

$$9 \quad \frac{\partial \bar{u}}{\partial t} + (\bar{u} \cdot \nabla) \bar{u} = -\frac{1}{\rho} \nabla P + \frac{\mu}{\rho} \nabla^2 \bar{u} + \vec{f} \quad (4)$$

$$10 \quad \nabla \cdot \bar{u} = 0 \quad (5)$$

11 , where \bar{u} is the flow field, ρ is the fluid density at a constant value, μ is the fluid viscosity,
 12 and \vec{f} is the gravity term. We created a three-dimensional computational domain that is
 13 similar to the GFS used for PIV measurement. A total of 80,784 grid cells was created. The
 14 rubber wall motion simulating an ACW was defined by an equation based on the Gaussian
 15 function.¹⁵ The minimum gap of the region occluded by an ACW was set to 3.0 mm. The
 16 boundary condition of the 4.0 x 4.0 mm inlet hole of the GFS was set as an outlet condition.
 17 All the other boundaries were set as a no-slip wall condition (i.e., the flow velocity near all
 18 walls was set to 0 mm/s). Since the gravity force is applied downward the Y-axis in Fig. 1 (a)
 19 in the actual experiment, we considered the gravity term also in CFD to calculate with the
 20 same flow condition as PIV experiment. The gravitational acceleration downward the Y-axis
 21 was set to 9.8 m/s². The time-differential term in Eq. 4 was approximated by forward
 22 differences with the dt set to 10⁻² s. A first-order upwind scheme was applied to solve the
 23 convection term in Eq. 4. A second-order central scheme was applied to the other terms in
 24 Eqs. 4 and 5. All equations were solved at each time step with a maximum of 20 iterations

1 using the SIMPLE-Consistent (SIMPLEC) method.²² The physical properties of liquid gastric
 2 contents presented in Table 1 were applied in the CFD calculations.

3 To simulate ACW in CFD, the equation of ACW ($ACW(x, y, t)$) was defined based on the
 4 previous study as follows:

$$5 \quad ACW(x, y, t) = A \exp\left[\left(\ln \varepsilon\right) \left\{ \left(\frac{2}{s}\right) \left((x - U_{ACW}t)\right)^2 + \left(\frac{2}{l}\right) x^{2m} + \left(\frac{2}{h}\right) y^{2n} \right\}\right] \quad (6)$$

6 where A is an amplitude of ACW, s is the wave width at the point of wave height ε , the
 7 natural number m and n are a parameter corresponding to the range where the ACW amplitude
 8 has a maximum value. l and h show the range along x - and y -axis, respectively, where ACW is
 9 generated.¹⁵ The amplitude A was set to 6.0 mm so that the minimum clearance of GFS is 3.0
 10 mm when ACW is generated. Since the wave width of ACW in PIV measurement is 60 mm,
 11 the parameter of wave width s was also set to 60 mm. The range where ACW is generated was
 12 114 mm x 30 mm (Fig. 1a: gray plane), corresponding $(l, h) = (114, 30)$. The values of ε , m ,
 13 and n were set to 0.01, 5, and 8 based on previous study.¹⁵ The U_{ACW} set in the calculations
 14 was the same as that used for PIV measurement ($U_{ACW} = 1.25, 2.5, 5.0$ mm/s).

15

16 **3. Results and discussion**

17 *3.1. Flow analysis using liquid gastric contents*

18 *3.1.1. Effect of fluid viscosity*

19 The flow-field in liquid gastric contents with different viscosities was quantitatively
 20 measured using GFS (Fig. 2). Though some noise vectors close to the rubber walls were
 21 observed due to the light refraction from rubber walls, the flow velocity of most noise vectors
 22 was quite low (less than 0.1 mm/s) so that it hardly affect the results of PIV. The U_{ACW} was set
 23 to 2.5 mm/s. The flow velocity distribution of water measured by PIV is presented in Fig.
 24 2a(i). The fluid inside GFS flowed against the direction of ACW (i.e., toward the pylorus).

1 This is called retroulsive flow.¹³ The flow velocity was greatest in the occluded region where
2 the rubber walls were compressed by rollers. The maximum flow velocity was 9.1 mm/s,
3 which was 3.6 times larger than the applied U_{ACW} . The eddy flow was also observed near the
4 walls behind the ACWs. The flow velocity distribution of water calculated by CFD is
5 presented in Fig. 2b(i). The retroulsive and eddy flows were observed in this case. A
6 maximum flow velocity of 10.4 mm/s was obtained in the occluded region. In addition, the
7 flow patterns depicted in Fig. 2 corresponded to the results obtained from lattice Boltzmann
8 calculation using the whole stomach structure,¹³ indicating that GFS can successfully simulate
9 intragastric flow in the human stomach.

10 Fluid viscosity hardly affected the intragastric flow patterns in the applied range of this
11 study (1 to 100 mPa s) for both PIV and CFD (Fig. 2a, b); the maximum flow velocity was
12 9.0 to 9.2 mm/s for PIV and 8.5 to 10.4 mm/s for CFD in the occluded region. However, the
13 tendency was the same between CFD (Fig. 2b(ii, iii)) and PIV, indicating that the intragastric
14 flow induced by peristalsis is independent of the viscosity of liquid gastric contents and that
15 stable mixing may take place in the actual stomach.

16

17 3.1.2. *Effect of ACW progression speed*

18 The flow-fields in water with different U_{ACW} values are indicated in Figs. 3a (PIV) and
19 3b (CFD). The flow patterns at U_{ACW} of 1.25 and 5.0 mm/s were almost the same as those at
20 2.5 mm/s in PIV and CFD. The range at which high flow velocity was observed increased as
21 U_{ACW} increased. Since flow velocity at U_{ACW} of 1.25 mm/s was quite low, a complex flow
22 derived from natural convection was observed (left-hand side of Fig. 3a(i)).

23 Figure 4 indicates the effects of fluid viscosity and U_{ACW} on maximum flow velocity in
24 the occluded region. In all U_{ACW} conditions, the maximum flow velocity in water ($\mu = 0.91$
25 mPa s) was slight higher than that of SS36 and SS56 ($\mu = 13.4$ mPa s and $\mu = 149$ mPa s,

1 respectively). This behavior can be derived from a rapid response to compression in the case
2 of water. The compression between ACW and the pylorus can be one of the driving forces of
3 retropulsive flow. The high fluidity of water can transmit this pressure faster than low fluidity
4 fluid such as SS36 and SS56 ($\mu = 13.4$ mPa s and $\mu = 149$ mPa s, respectively), which can
5 promote the high flow velocity in case of water.

6 There was also a slight difference of maximum flow velocity between PIV and CFD in
7 the case of water ($\mu = 0.91$ mPa s). This difference is due to the high fluidity of water, so that
8 making difficult to control of experimental flow conditions. For instance, in case of $U_{ACW} =$
9 1.25 and 2.5 mm/s, the maximum flow velocity obtained in PIV was slightly lower than that
10 of CFD. For $U_{ACW} = 5.0$ mm/s, the maximum flow velocity obtained in PIV was higher than
11 that of CFD in the condition. On the other hand, for SS36 and SS56, the difference of
12 maximum flow velocity between PIV and CFD was narrow, which is due to their lower
13 fluidity ($\mu = 13.4$ mPa s and 149 mPa s, respectively).

14 These results indicate that the maximum flow velocity obtained by PIV corresponded
15 well with that of CFD calculation. Also, the correspondence of flow-field between
16 experimental and numerical approaches suggests that flow-field was successfully analyzed in
17 each condition.

18 The maximum flow velocity was four times higher than the applied speed of ACWs in
19 all results. The Reynolds number (Re) was estimated according to Eq. 7:

$$20 \quad Re = \frac{\rho UL}{\mu} \quad (7)$$

21 , where the hydraulic diameter of the occluded region in GFS (5.5 mm) was applied to L as
22 the characteristic length. The characteristic flow velocity U was set to the maximum flow
23 velocity for each liquid gastric content under different U_{ACW} values. Re was estimated
24 between 0.203 ($U_{ACW} = 1.25$ mm/s, filled with SS56) and 125 ($U_{ACW} = 5.0$ mm/s, filled with

1 water). The maximum Re of 125 indicated that the flow-field inside GFS was laminar flow.
2 These experimental and numerical data strongly suggest that intragastric flow in the actual
3 human stomach is also laminar at least for liquid food digestion. Retropulsive flow may
4 contribute to physical digestion of food by mildly mixing gastric contents.

5

6 3.1.3. Shear force analysis in liquid gastric contents

7 Even though our previous study shows the numerical shear force induced by peristalsis,¹⁵
8 there is still no experimental shear force data. Then, the absolute value of the shear rate ($|\dot{\gamma}|$)
9 that acts on liquid gastric contents was estimated using Eq. 2 and the flow-field data obtained
10 from PIV measurement. A typical example of shear rate distribution for water is presented at
11 the top of Fig. 5. Bimodal peaks were observed along the rubber walls in the occluded region,
12 reaching the maximum shear rate of 16 s^{-1} . The shear rate distribution was almost the same,
13 regardless of fluid viscosity and other flow conditions (data not shown).

14 Fig. 6 indicates the maximum shear rate and shear stress obtained in the occluded region
15 as a function of fluid viscosity and U_{ACW} . As shown in Fig. 6a, fluid viscosity did not affect
16 the maximum shear rate for $\mu = 13.4$ and 149 mPa s at U_{ACW} of 2.5 and 5.0 mm/s. However,
17 the maximum shear rate for $\mu = 0.91 \text{ mPa s}$ exceeded that for water containing starch syrup
18 by 34%. This tendency was assumed to be derived from the high fluidity of water, which
19 induces more drastic variation of flow velocity. For $U_{ACW} = 1.25 \text{ mm/s}$, the maximum shear
20 rate hardly varied within the range of fluid viscosity applied; therefore, it was assumed that
21 the applied U_{ACW} was too slow to vary flow velocity, even low fluid viscosity. The maximum
22 shear rate also increased with increasing U_{ACW} . When the U_{ACW} was increased two-fold (1.25
23 to 2.5 mm/s or 2.5 to 5.0 mm/s), the maximum shear rate also increased approximately twice.
24 This tendency was similar to the relationship between U_{ACW} and maximum flow velocity in
25 the occluded region, which showed the dependency of shear rate on intragastric flow-field.

1 Since all fluids applied in this study were Newtonian¹⁸, all shear stresses (σ) were
2 estimated by multiplying the absolute value shear rate ($|\dot{\gamma}|$) by fluid viscosity (μ) according to
3 Eq. 3 (Fig. 6b). In spite of the slight difference of maximum shear rate between water and
4 starch syrup solutions (SS36 and SS56), the maximum shear stress increased almost linearly
5 with fluid viscosity. This is because the variance of maximum shear rate in each condition
6 was enough small than that of applied range of viscosity so that the viscosity effects on shear
7 stress was dominant, since the shear stress is the product of viscosity and shear rate (see Eq.
8 3). The difference of maximum shear rate was at most 1.5 times ($11 - 17 \text{ s}^{-1}$) in the same
9 condition of U_{ACW} , whereas applied range of viscosity was approximately 150 times ($0.91 -$
10 149 mPa s).

11 In all shear force analysis using liquid gastric contents, the shear rate, which is the
12 potential force for grinding foods, was on the order of 10^1 s^{-1} , which is much lower than that
13 of the general homogenizer (10^3 to 10^4 s^{-1}). This result indicates that shear force due to fluid
14 flow could be considerably low for breaking down food particles.

15

16 3.2. Flow analysis using liquid-solid gastric contents

17 3.2.1. Measurement of flow-field around model solid food particles using PIV

18 Figure 7 indicates the flow velocity distribution around the model solid food particles
19 (plastic beads) in the occluded region, with the volume ratio of model solid food particles
20 below 5%. When ACW progressed from left to right (toward the pylorus), the model solid
21 food particles moved in the opposite direction against ACW according to the motion of the
22 rubber walls and liquid phase. The direction of velocity vectors dynamically changed near the
23 model solid food particles with relatively high flow velocity. The tendency of the flow-field
24 was almost the same even if the viscosity of liquid gastric contents was changed. The mobility
25 of the model solid food particles became low when viscous fluid was applied ($\mu = 13.4, 149$

1 mPa s) because of low fluidity. The maximum flow velocity near the surface of the model
2 solid food particles was 12 mm/s in the water flow system, which was similar to that of the
3 flow system of $\mu = 13.4$ and 149 mPa s, with less than a 10% difference in flow velocity.

4 To determine the effect of the amount of model solid food particles on flow velocity, the
5 average flow velocity near the model solid food particles was measured by tracking each
6 tracer particle within the analyzed region (Fig. 8a). The average flow velocity increased to the
7 volume ratio of 12.5%, reaching a maximum value of 9.3 mm/s; then the flow velocity
8 decreased to a volume ratio exceeding 12.5%. This tendency was assumed to be based on the
9 balance between the fluid pressure gradient and the volume ratio of liquid phase. In general, a
10 narrower flow pass generates a higher flow velocity at the same fluid pressure. Thus, with a
11 volume ratio below 12.5%, an increase in flow velocity can be caused by a decrease in flow
12 pass because of increased model solid food particles. However, with a volume ratio above
13 12.5%, the volume ratio of liquid phase became insufficient due to the decreased fluid
14 pressure gradient, which is the indicator of flow velocity (see Eq. 4). This can affect more
15 strongly to the decrease of flow velocity compared to the effect of flow pass decrease in the
16 condition of volume ratio below 12.5%.

17

18 3.2.2. *Shear force analysis in liquid-solid gastric contents*

19 The absolute value of the shear rate ($|\dot{\gamma}|$) in liquid-solid gastric contents was estimated
20 using Eq. 2, and the results of the flow-field are depicted in Fig. 7. Figure 9 presents the
21 intragastric shear rate profile with flow-field information in the occluded region. A high shear
22 rate was observed near the rubber walls of GFS, similar to the results for liquid gastric
23 contents. The shear rate was also high for the upper part of the model solid food particles,
24 since the flow velocity gradient was high on their surfaces. The shear rate profile was almost
25 independent of fluid viscosity (Fig. 9). The maximum shear rate for the top of the model solid

1 food particles was on the order of 10 s^{-1} . These results indicate that maximum shear force
2 induced by gastric peristalsis is low even in the presence of solid foods.

3 Concerning numerical calculation, our previous study shows the numerical flow-field
4 and shear rate data in single phase obtained by CFD, but it is our understanding that until now
5 there is no experimental data of shear rate in single phase, intragastric flow-field and shear
6 rate data in two phases. Thus, the flow-field around the model solid food particles obtained in
7 this study provides a new insight of physical digestion phenomena in stomach.

8

9 *3.3. Hydrodynamic effects on food digestion induced by gastric peristalsis*

10 The physical digestive effects in the human stomach can be divided into mixing that
11 promotes the chemical reaction of gastric juice, and grinding that reduces the size of bulk
12 solid foods. Regarding the mixing effect, the flow-fields in both liquid and liquid-solid gastric
13 contents obtained in this study suggest the possible motion of gastric contents, which may
14 promote mixing of gastric juice and foods in gastric digestion. The mixing flow in the
15 stomach is considered to be “mild” since the maximum flow velocity was on the order of 1 to
16 10 mm/s. In contrast, the flow velocity of commonly used homogenizers is on the order of 10^3
17 mm/s. Mild intragastric flow could also cause a locally unmixed region where α -amylase
18 derived from saliva is still active, due to the insufficient decrease of pH, and promotes
19 carbohydrate disintegration.

20 However, low shear force was observed in both this study (Fig. 5) and a previous work.¹⁵
21 This result indicates that hydrodynamic shear force induced by gastric peristalsis might not
22 cause mechanical grinding of bulk foods. Compression stress in the occluded region is
23 assumed to be another force that plays an important role in food grinding.¹ This force is
24 derived from mechanical compression stress resulting from contraction of the gastric wall.
25 Compression stress was reported in several *in vivo* studies, with a measured range of 5 to 70

1 kPa.^{23,24} Further investigation is needed to clarify the physical digestion effects of this
2 compression stress in the human stomach.

3

4 **4. Conclusions**

5 The intragastric flow induced by gastric peristalsis was reasonably simulated using a
6 human GFS. Retropulsive flow against the direction of peristalsis was observed in liquid
7 gastric contents using PIV and CFD. When standard values of peristalsis speed in healthy
8 adults ($U_{ACW} = 2.5$ mm/s) was applied, a maximum flow velocity of 10 mm/s was observed in
9 the most occluded region due to peristalsis, suggesting laminar intragastric flow in liquid
10 gastric contents. The PIV results demonstrated that the flow-field in liquid-solid gastric
11 contents was dynamically changed at the surface of model solid food particles. The maximum
12 flow velocity in the liquid phase of liquid-solid gastric contents was almost the same as that in
13 liquid gastric contents. The maximum flow velocity in the liquid phase was independent of
14 fluid viscosity. The use of GFS and PIV enabled us to obtain the shear force profile in gastric
15 contents. The maximum shear rate in liquid and liquid-solid gastric contents was on the order
16 of 10 s^{-1} , indicating that it is difficult to disintegrate food particles solely by hydrodynamic
17 shear force induced by gastric peristalsis. Our findings provide a new insight of physical
18 digestion phenomena in stomach.

19

20 **Acknowledgment**

21 This work was partially supported by Grant-in-Aid Japan Society for the Promotion of
22 Science (JSPS) Fellows 25·1035.

23

24 **References**

25 1. F. Kong and R. P. Singh, Disintegration of solid foods in human stomach, *J. Food Sci.*,

- 1 2008, **73**, R67–R80.
- 2 2. W. Ajaj, S. C. Goehde, N. Papanikolaou, G. Holtmann, S. G. Ruehm, J. F. Debatin and T.
3 C. Lauenstein, Real time high resolution magnetic resonance imaging for the assessment
4 of gastric motility disorders, *Gut*, 2004, **53**, 1256–1261.
- 5 3. W. Schwizer, A. Steingoetter and M. Fox, Magnetic resonance imaging for the assessment
6 of gastrointestinal function, *Scand. J. Gastroenterol.*, 2006, **41**, 1245–1260.
- 7 4. B. Abrahamsson, A. Pal, M. Sjoberg, M. Carlsson, E. Laurell and J. G. Brasseur, A novel
8 in vitro and numerical analysis of shear-induced drug release from extended-release
9 tablets in the fed stomach, *Pharm. Res.*, 2005, **22**, 1215–1226.
- 10 5. D. J. McClements and Y. Li, Review of in vitro digestion models for rapid screening of
11 emulsion-based systems, *Food Funct.*, 2010, **1**, 32-59.
- 12 6. F. Kong and R. P. Singh, A Model Stomach System to Investigate Disintegration Kinetics
13 of Solid Foods during Gastric Digestion, *J. Food Sci.*, 2008, **73**, E202–E210.
- 14 7. G. A. van Aken, E. Bomhof, F. D. Zoet, M. Verbeek and A. Oosterveld, Differences in *in*
15 *vitro* gastric behaviour between homogenized milk and emulsions stabilised by Tween 80,
16 whey protein, or whey protein and caseinate, *Food Hydrocoll.*, 2011, **25**, 781-788.
- 17 8. Z. Wang, M. A. Neves, I. Kobayashi, K. Uemura and M. Nakajima, Preparation,
18 characterization, and in vitro gastrointestinal digestibility of oil-in-water emulsion-agar
19 gels, *Biosci. Biotechnol. Biochem.*, 2013, **77**, 467-474.
- 20 9. M. J. van der Werf and K. Venema, Bifidobacteria: Genetic Modification and the Study of
21 Their Role in the Colon, *J. Agric. Food Chem.*, 2001, **49**, 378-383.
- 22 10. A. Mercuri, A. Lo Curto, M. S. J. Wickham, D. Q. M. Craig and S. A. Barker, Dynamic
23 gastric model (DGM): a novel in vitro apparatus to assess the impact of gastric digestion
24 on the droplet size of self-emulsifying drug-delivery systems, *J. Pharm. Pharmacol.*,
25 2008, **60**, A-2.

- 1 11. A. Guerra, L. Etienne-Mesmin, V. Livrelli, S. Denis, S. Blanquet-Diot and M. Alric,
2 Relevance and challenges in modeling human gastric and small intestinal digestion,
3 *Trends Biotechnol.*, 2012, **30** (11), 591-600.
- 4 12. F. Kong and R. P. Singh, A human gastric simulator (HGS) to study food digestion in
5 human stomach, *J. Food Sci.*, 2010, **75**, E627–E635.
- 6 13. A. Pal, K. Indireskumar, W. Schwizer, B. Abrahamsson, M. Fried, and J. G. Bresseur,
7 Gastric flow and mixing studied using computer simulation, *Proc. R. Soc. B*, 2004, **271**,
8 2587-2594.
- 9 14. M. J Ferrua and R. P. Singh, Modeling the fluid dynamics in a human stomach to gain
10 insight of food digestion, *J. Food Sci.*, 2010, **75**, R151–R162.
- 11 15. H Kozu, I. Kobayashi, M. Nakajima, K. Uemura, S. Sato and S. Ichikawa, Analysis of
12 flow phenomena in gastric contents induced by human gastric peristalsis using CFD, *Food*
13 *Biophys.*, 2010, **5**, 330-336.
- 14 16. Z. Xue, M. J. Ferrua and R. P. Singh, Computational fluid dynamics modeling of granular
15 flow in human stomach, *Alimentos Hoy*, 2012, **21**, 3-14.
- 16 17. L. Marciani, P. A. Gowland, R. C. Spiller, P. Manoj, R. J. Moore, P. Young, S. Al-Sahab,
17 D. Bush, J. Wright and A. J. Fillery-Travis, Gastric response to increased meal viscosity
18 assessed by echo-planar magnetic resonance imaging in humans, *J. Nutr.*, 2000, **130**,
19 122–127.
- 20 18. S. Iwata, Y. Yamada, T. Takashima and H. Mori, Pressure-oscillation defoaming for
21 viscoelastic fluid, *J. Non-Newtonian Fluid Mech.*, 2007, **151**, 30-37.
- 22 19. M.L. Jalabert-Malbos, A. Mishellany-Dutour, A. Woda, M.A. Peyron, Particle size
23 distribution in the food bolus after mastication of natural foods, *Food Qual. Prefer.*, 2007,
24 **18**, 803–812.
- 25 20. C. T. Crowe, M. Sommerfeld and Y. Tsuji, in *Multiphase flows with droplets and*

- 1 *particles*, CRC Press, NY, 1998, pp. 24.
- 2 21. J. Westerweel, Efficient detection of spurious vectors in particle image velocimetry, *Exp.*
3 *Fluids*, 1994, **16**, 236-247.
- 4 22. J. P. van Doormal and G. D. Raithby, Enhancement of the SIMPLEC method for
5 predicting incompressible fluid flows, *Numer. Heat Tr. Part B*, 1984, **7**, 147–163.
- 6 23. L. Marciani, P. A. Gowland, A. Fillery-Travis, P. Manoj, J. Wright, A. Smith, P. Young, R.
7 Moore and R. C. Spiller, Assessment of antral grinding of a model solid meal with
8 echo-planar imaging, *Am. J. Physiol. Gastrointest. Liver Physiol.*, 2001, **280**, G844–G849.
- 9 24. M. Kamba, Y. Seta, A. Kusai and M. Ikeda, A unique dosage form to evaluate the
10 mechanical destructive force in the gastrointestinal tract, *Int. J. Pharm.*, 2000, **208**, 61–70.
- 11
- 12

1 Table and Figure Captions

2 **Table 1.** Physical properties of each component in liquid and liquid-solid gastric contents.

3 **Fig. 1.** (a) Three-dimensional schematic diagram of a human Gastric Flow Simulator (GFS).
4 (b) Schematic top view of the GFS system. (c) Search plane images from the cross-sectional
5 view (x - y plane). The minimum clearance between deformed rubber walls is 3.0 mm.

6 **Fig. 2.** Visualized PIV and CFD results for the flow-field of liquid gastric contents with
7 different viscosities induced by peristalsis at U_{ACW} of 2.5 mm/s. (a) PIV data. (b) CFD data.

8 **Fig. 3.** Visualized PIV and CFD results for the effect of U_{ACW} on flow-field of Milli-Q water.
9 (a) PIV data. (b) CFD data.

10 **Fig. 4.** Effect of the liquid viscosity and U_{ACW} on the maximum flow velocity in the
11 occluded region obtained by PIV measurement (closed keys) and CFD calculation (open
12 keys). The U_{ACW} values applied are 1.25 mm/s (diamond), 2.5 mm/s (rectangle), and 5.0 mm/s
13 (circle).

14 **Fig. 5.** Shear rate (γ) distribution (top) and flow-field (bottom) of water in the GFS at U_{ACW}
15 of 2.5 mm/s. Dotted curves are rubber walls of the GFS. $||$ denotes the absolute value of the
16 shear rate. The bottom image is the same as in Fig. 2a(ii).

17 **Fig. 6.** Effect of liquid viscosity and U_{ACW} on the maximum shear rate (a) and maximum
18 shear stress (b) acting on liquid gastric contents. The U_{ACW} values applied are 1.25 mm/s
19 (diamond), 2.5 mm/s (rectangle), and 5.0 mm/s (circle).

20 **Fig. 7.** Visualized PIV results for the flow-field around the model solid food particles in the
21 GFS. White dotted curves denote rubber walls of the GFS.

22 **Fig. 8.** Effect of volume rate of the model solid food particles on average flow velocity
23 inside the analyzed region. The location and size of the region are depicted in (a). The average
24 velocities in (b) were estimated based on the motion of each tracer particle inside the analyzed
25 region ($n = 15$). Each error bar stands for the standard deviation.

- 1 **Fig. 9.** Shear rate distribution and flow-field around the model solid foods in the GFS.
- 2 White dotted curves denote rubber walls of the GFS. $||$ denotes the absolute value of the shear
- 3 rate. The length of vectors represents the flow speed of the liquid phase.

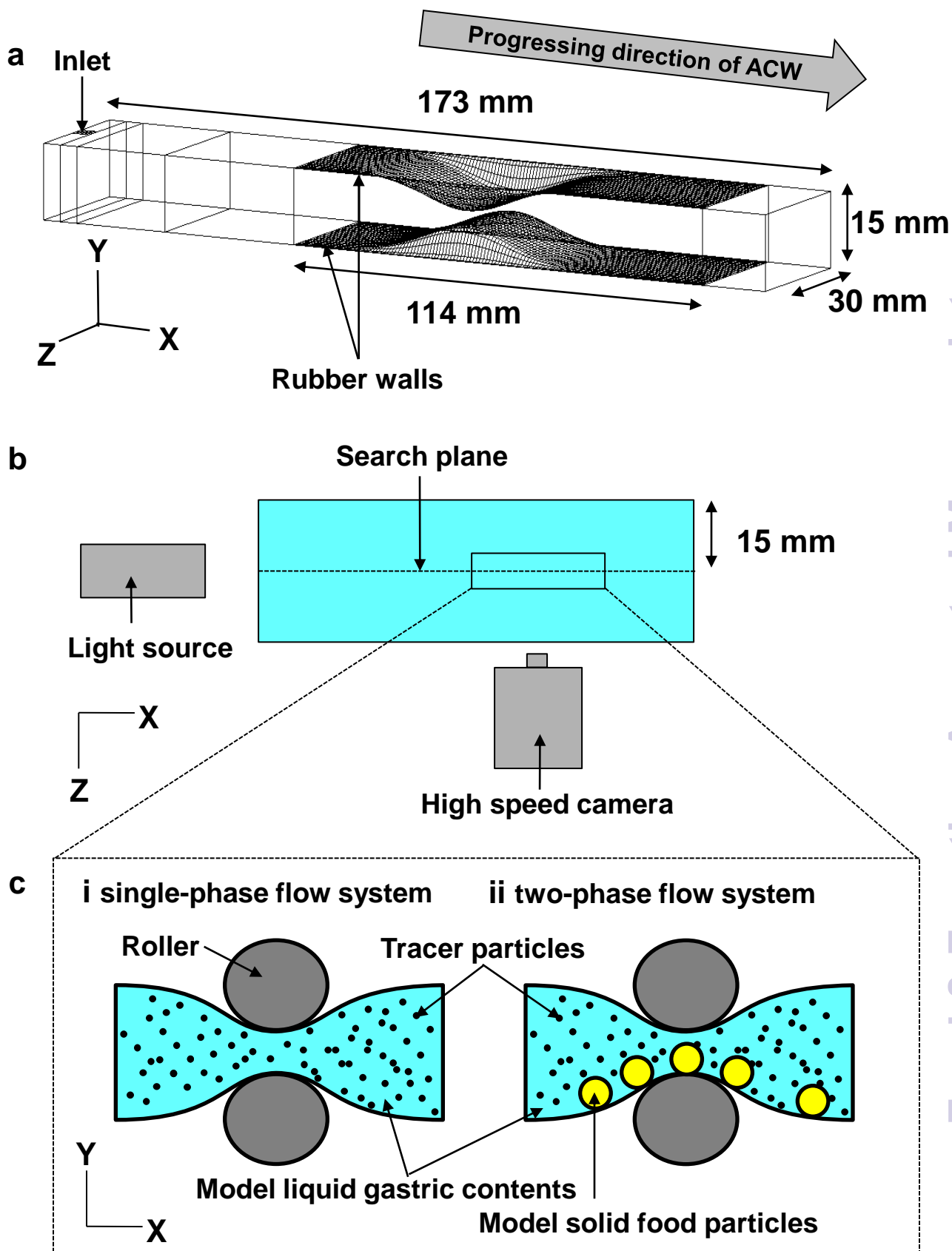
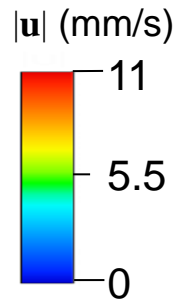
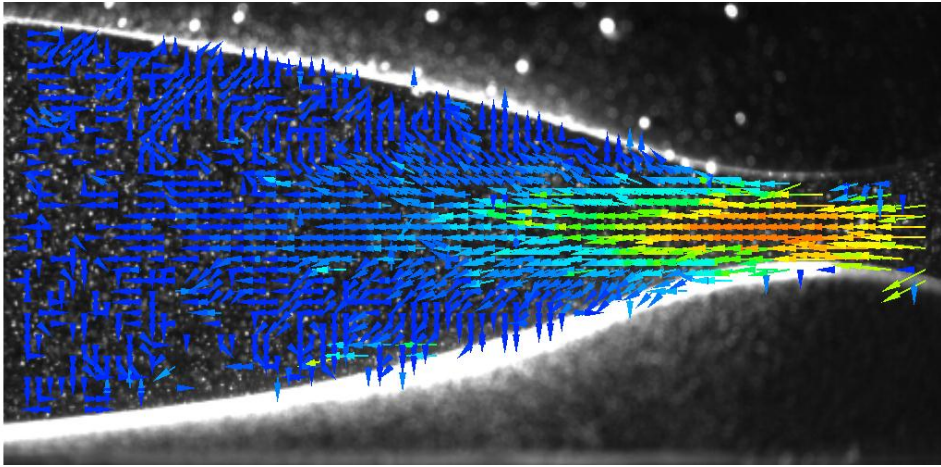
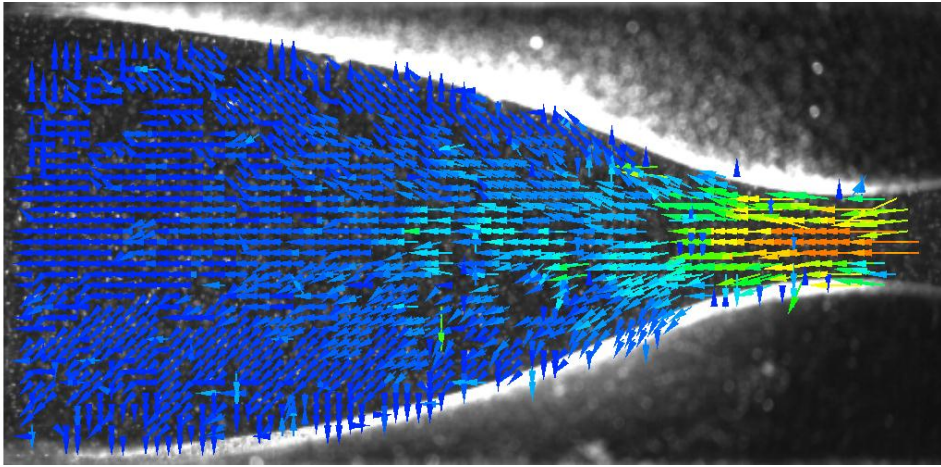


Fig. 1

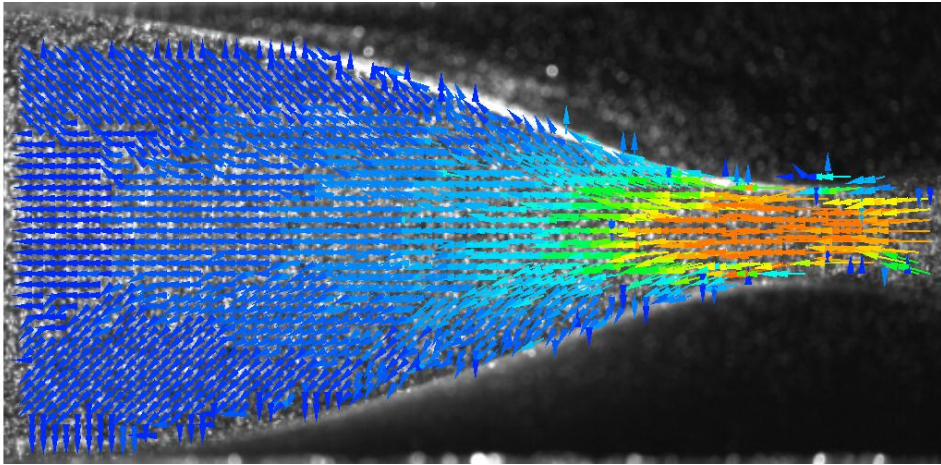
i water



ii SS36



iii SS56



3 mm

Progressing direction of ACW 

Fig. 2a

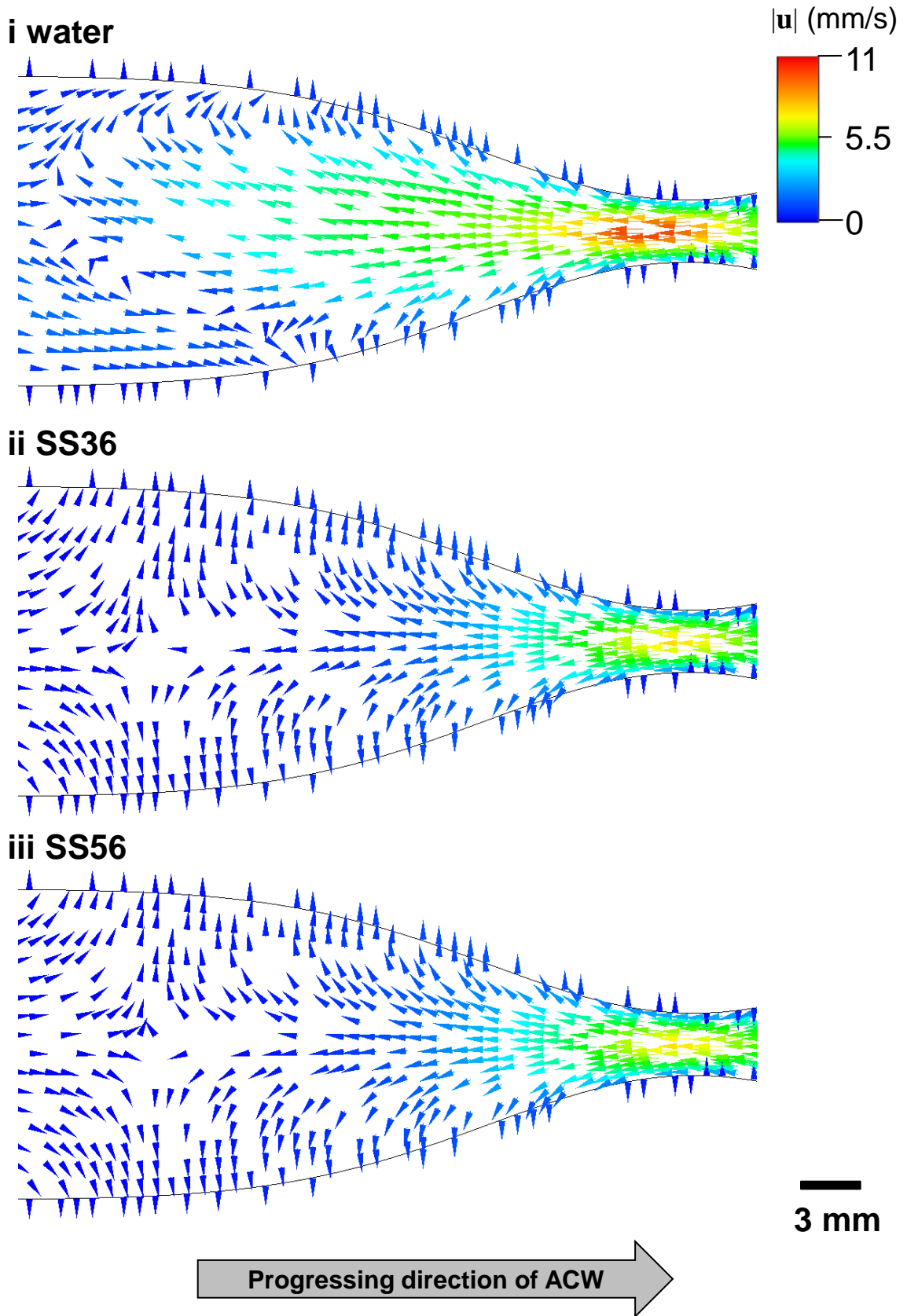
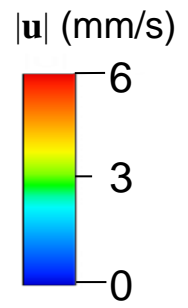
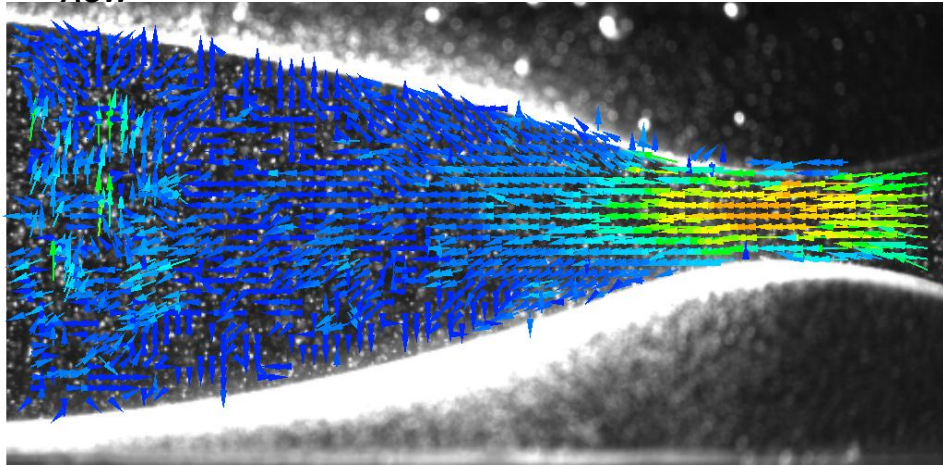
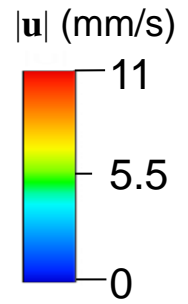
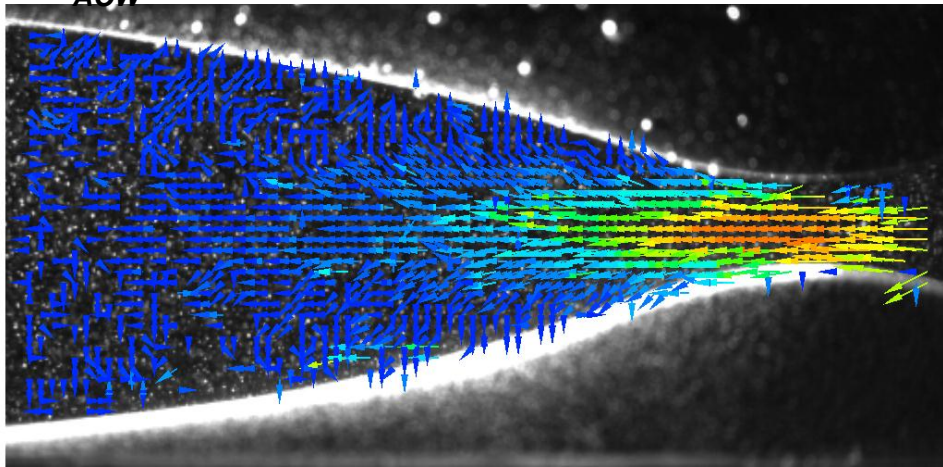


Fig. 2b

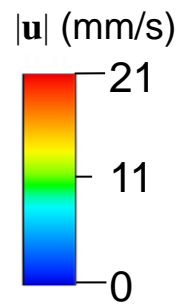
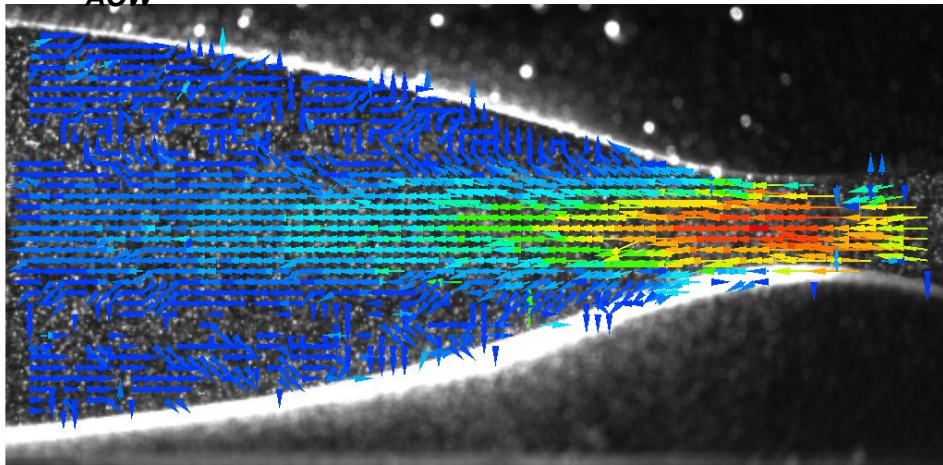
i $U_{ACW} = 1.25$ mm/s



ii $U_{ACW} = 2.5$ mm/s



iii $U_{ACW} = 5.0$ mm/s



3 mm

Progressing direction of ACW

Fig. 3a

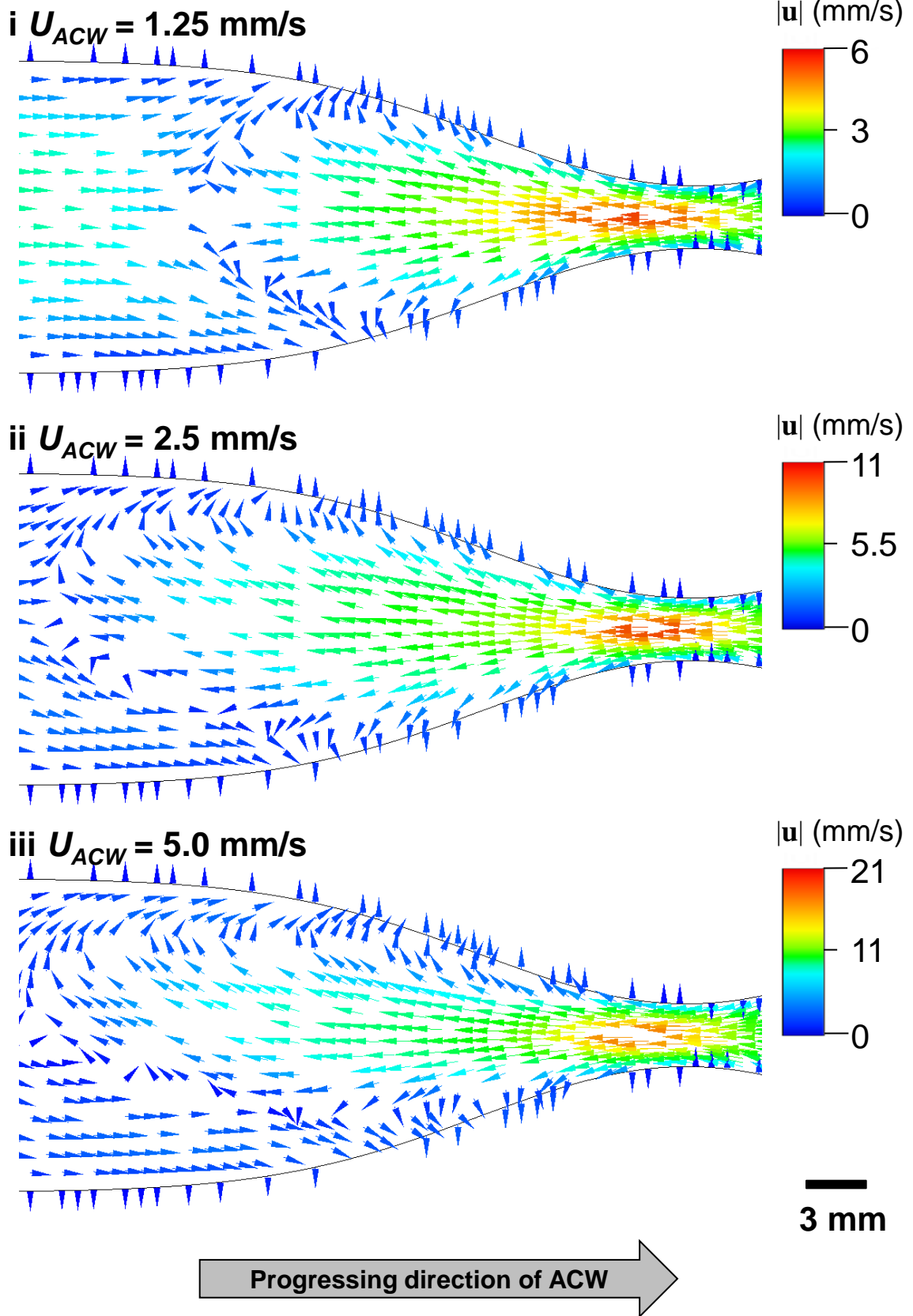
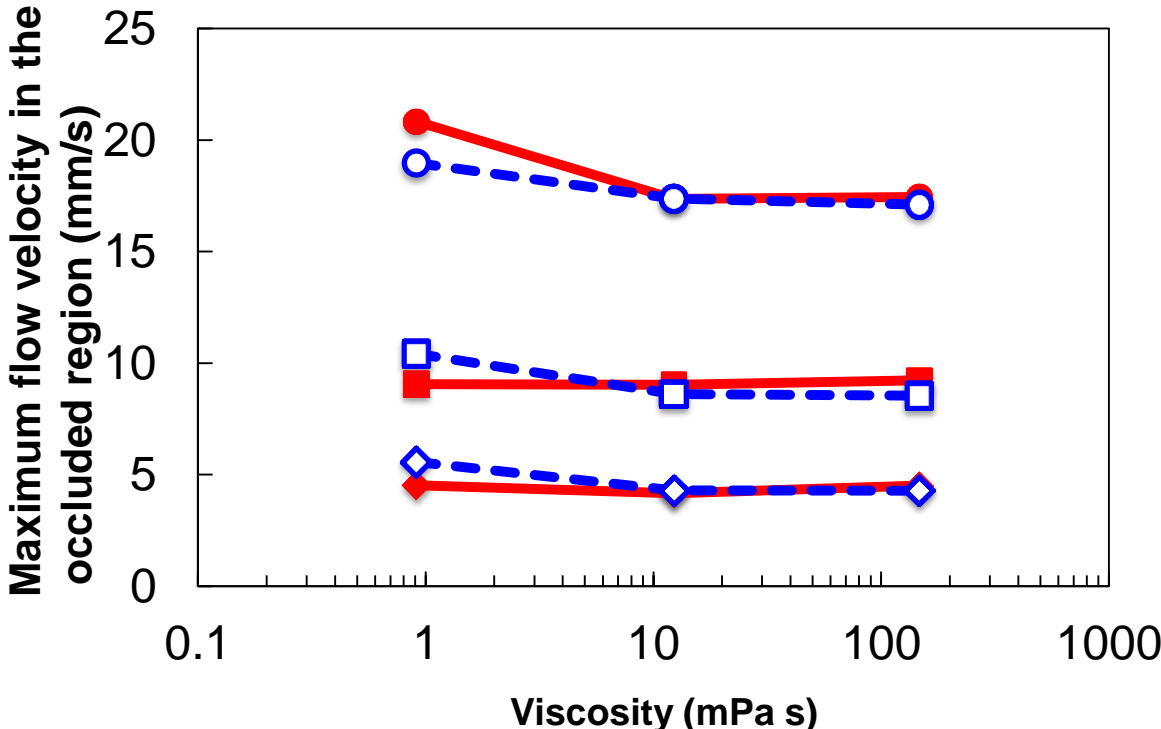


Fig. 3b



Food & Function Accepted Manuscript

Fig. 4

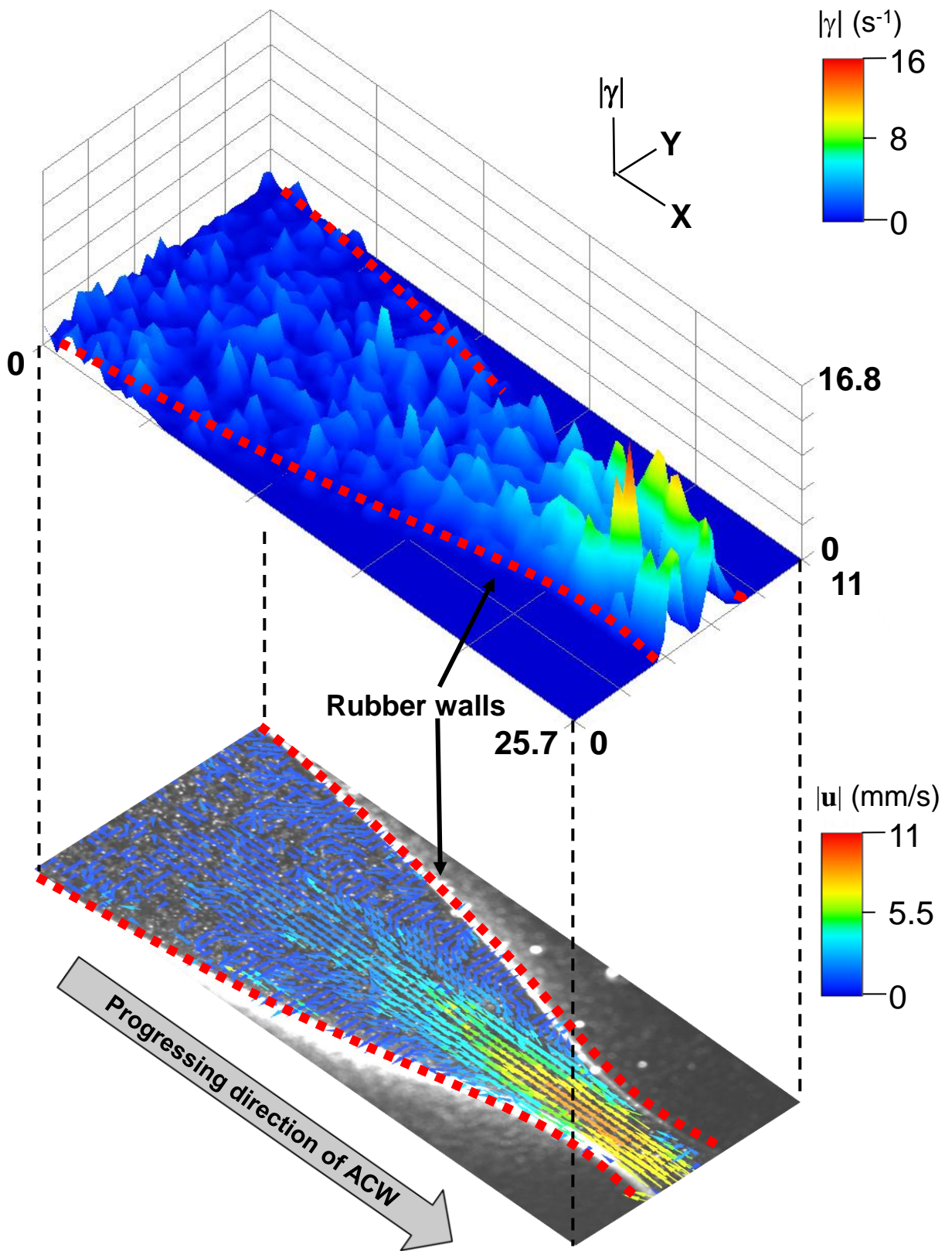


Fig. 5

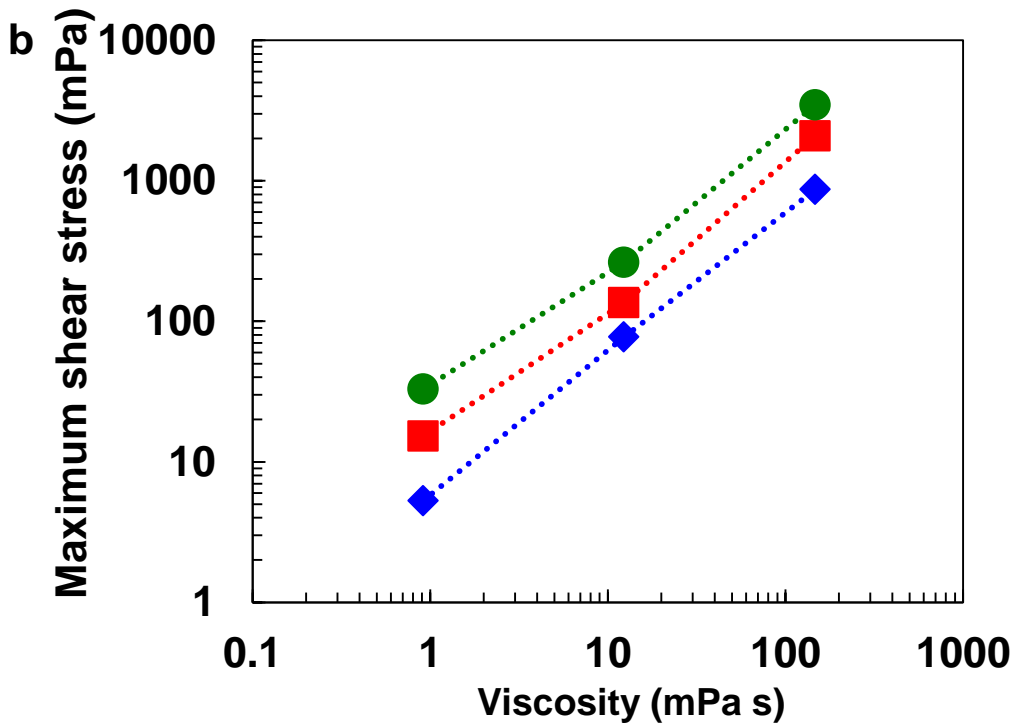
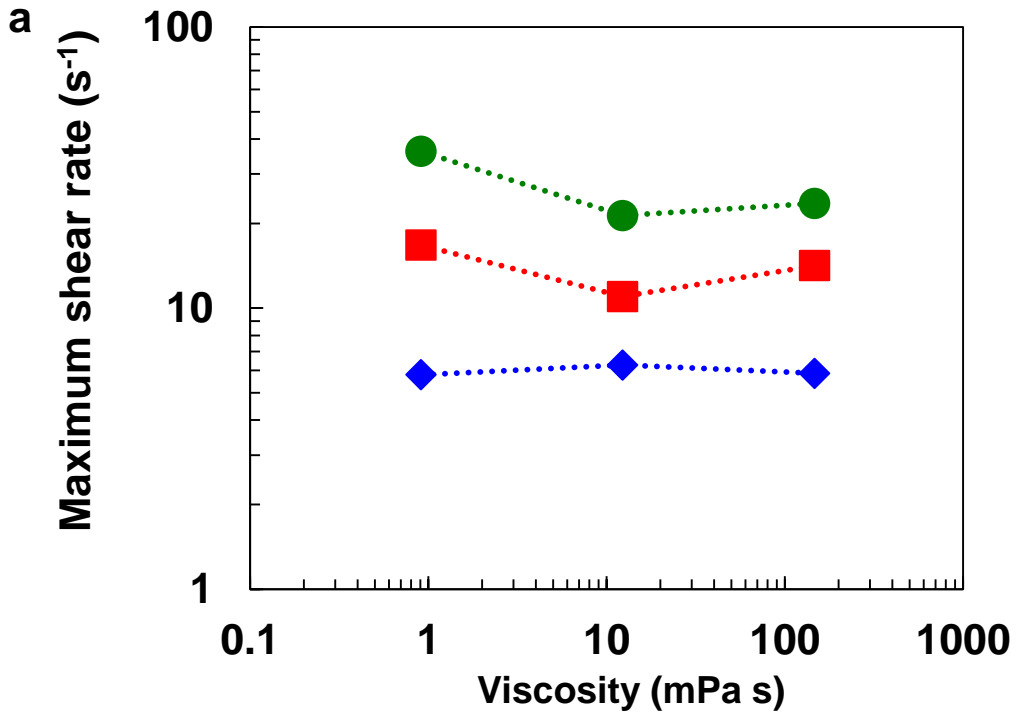
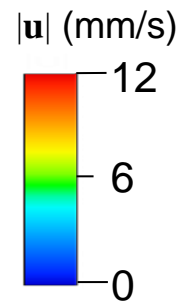
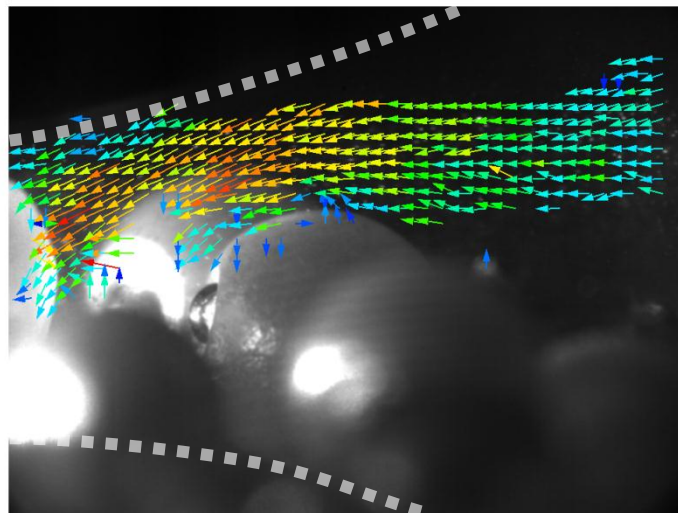
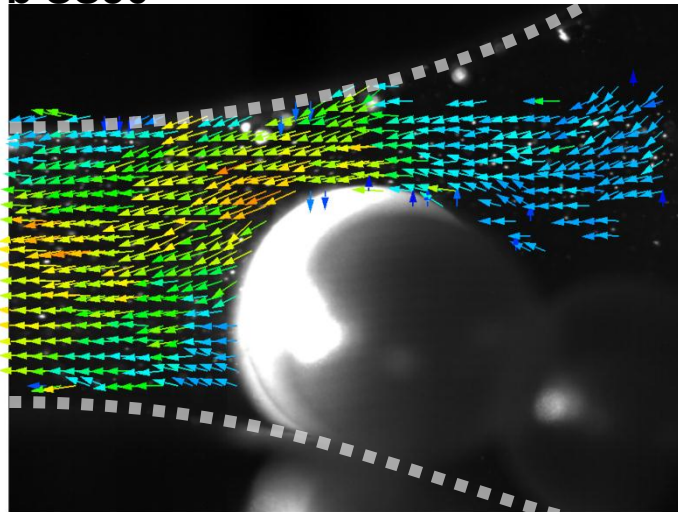


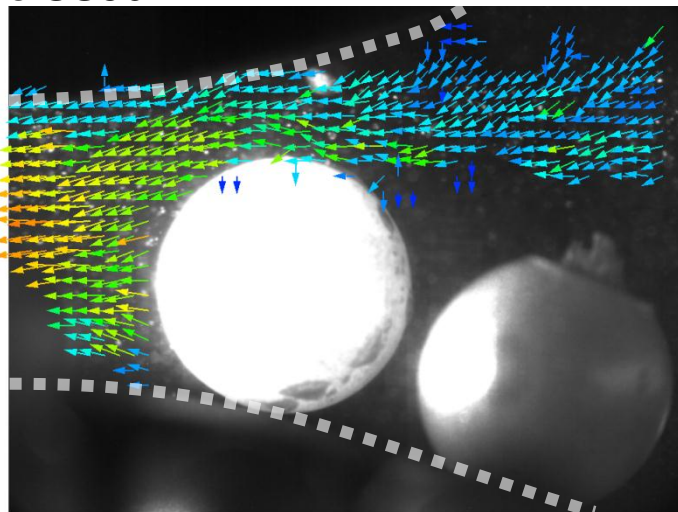
Fig. 6



b SS36



c SS56



1 mm

Progressing direction of ACW

Fig. 7

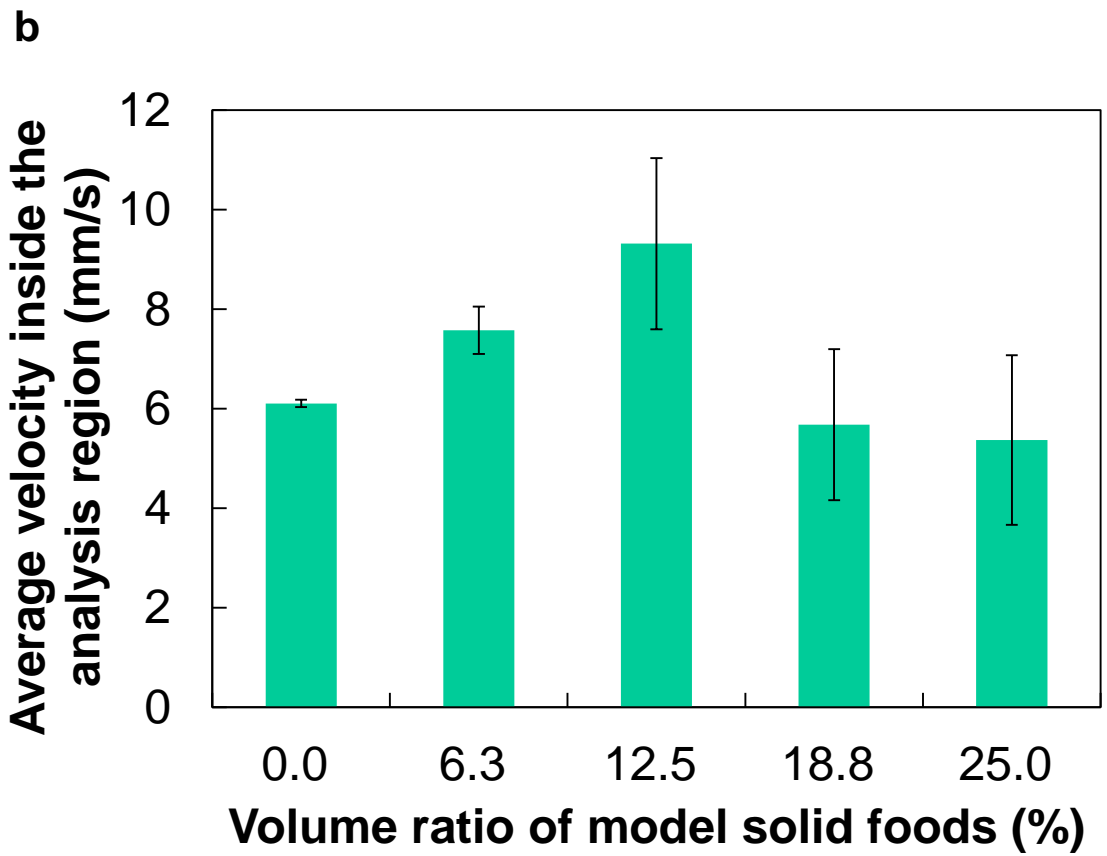
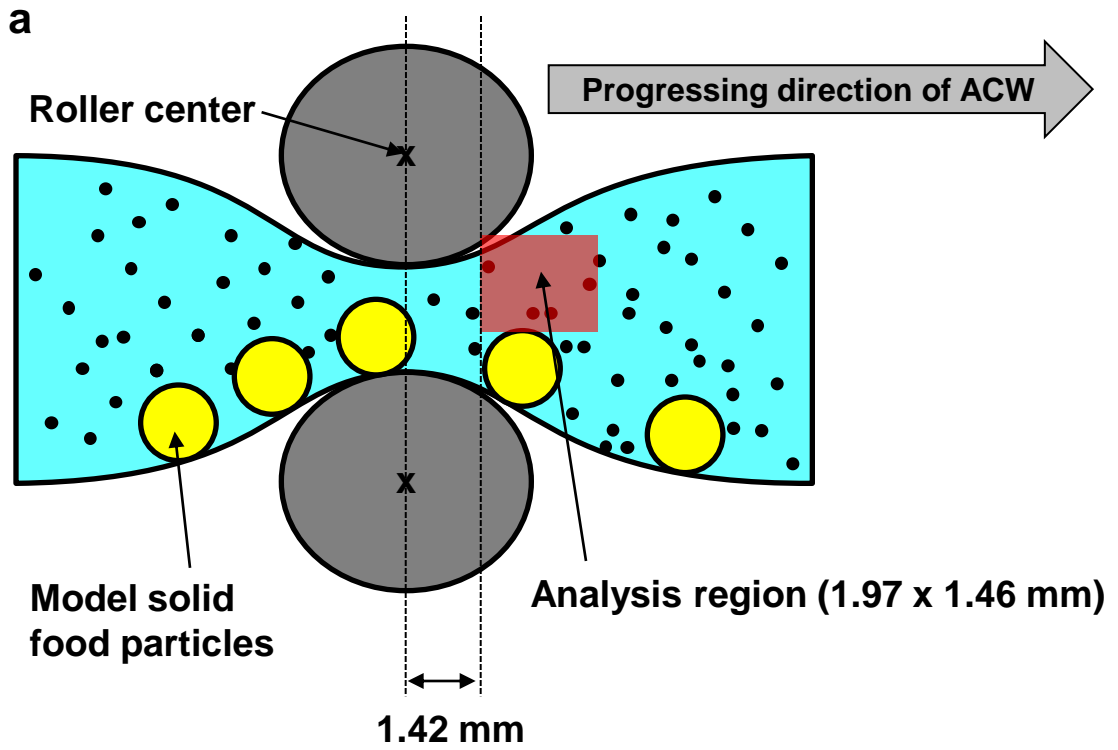
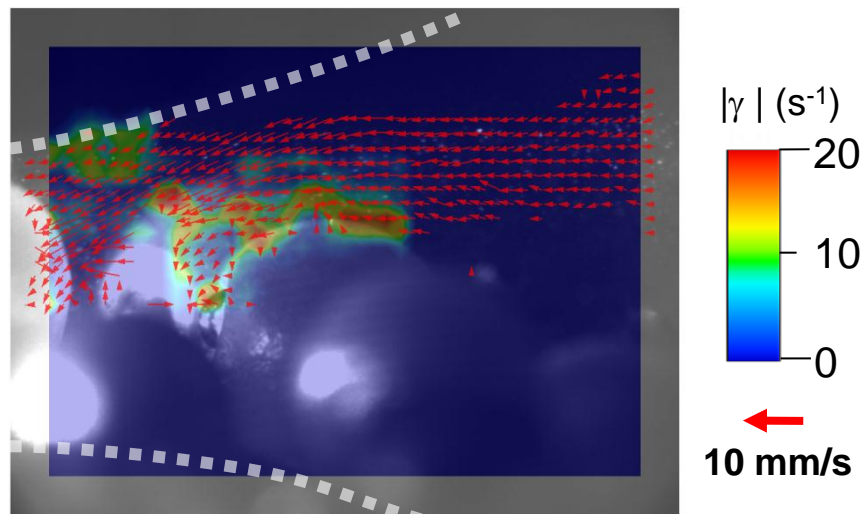
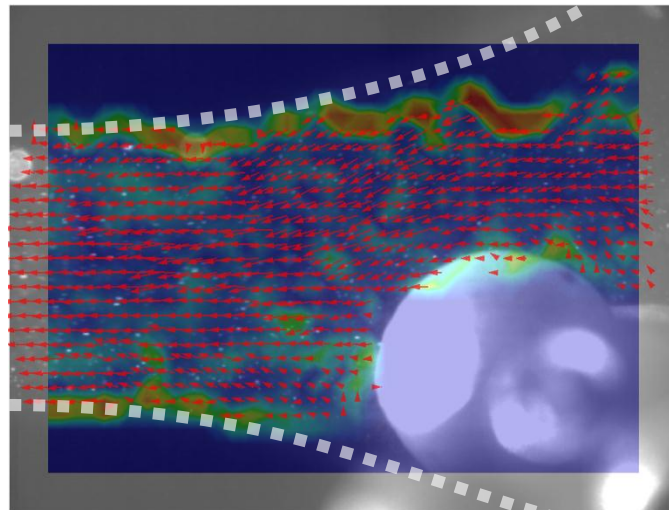


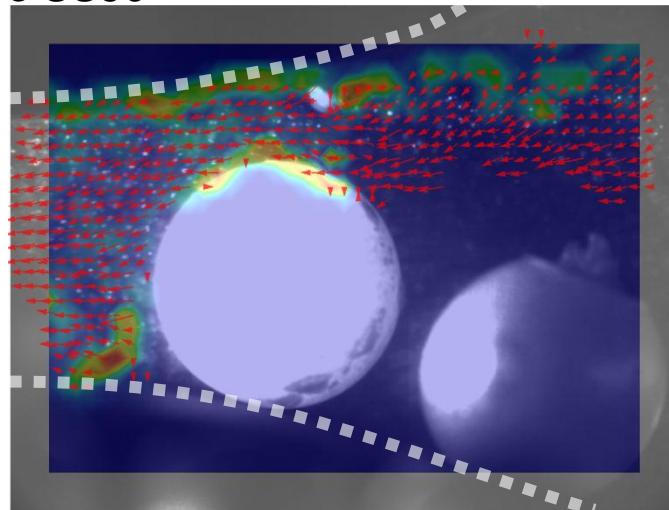
Fig. 8



b SS36



c SS56



1 mm

Progressing direction of ACW

Fig. 9

Table 1

Gastric contents	Liquid components				Solid component
	Symbol	Composition	Density (kg/m ³)	Viscosity (mPa s)	
Liquid (single- phase)	Water	Milli-Q	997.0	0.910	-
	SS36	Starch syrup (36% (v/v))	1188	13.4	-
	SS56	Starch syrup (56% (v/v))	1292	149	-
Liquid- solid (two- phase)	Water	Milli-Q	997.0	0.910	Plastic beads
	SS36	Starch syrup (36% (v/v))	1188	13.4	(ϕ 3.0 mm)
	SS56	Starch syrup (56% (v/v))	1292	149	(< 25% (v/v))